Large-eddy simulation of a turbulent helium-air plume using the nLES method

By G. C. Burton

1. Motivation and objective

The turbulent plume is created by the injection of a fluid jet into a higher-density ambient fluid, usually with the gravity vector opposing the direction of jet inflow. The plume is important to a diverse range of engineering and scientific applications such as industrial pool fires, atmospheric exhaust phenomena like smokestacks, gas releases in geothermal events and the cooling of stored fluids in various industrial processes. There is thus great interest in developing a better understanding of how these flows evolve.

Several factors, however, make the turbulent plume particularly difficult to study. In the plume, there is a rapid transition of the flow from laminar to fully turbulent, usually within a few inlet diameters of the source. Once turbulent, plumes are characterized by large-scale vorticity created as the result of buoyancy and shear forces arising from the interaction of the jet with the ambient fluid. The misalignment of the pressure and density gradients near the edges of the inlet gives rise to baroclinic torque, $\Gamma_{bar} \equiv -\left(\nabla\rho \times \nabla p\right)/\rho^2$, which produces Rayleigh-Taylor instabilities at the two-fluid interface. In addition, Kelvin-Helmholtz instabilties arise from shearing at these interfaces. Both the RT and KH instabilities produce inverse cascades of kinetic and scalar energies, which energize larger-scale structures as the plume rises from its base. The interaction of the buoyancy forces with the vorticity also generates a characteristic "puffing" motion, by which entrained ambient fluid periodically forces aloft a blob of lighter fluid accumulating near the plume base. However, the exact mechanism giving rise to this puffing cycle is a matter of current debate. In cases where the Reynolds and Richardson numbers $Ri \equiv (\rho_\infty - \rho_p)gD/(\rho_\infty U_p^2)$ are large enough, these unstable modes may be altered by intermittent secondary torroidal vortices that make the puffing rate irregular, and which amplify the entrainment rates and thus strongly alter plume dynamics overall.

Numerical study of turbulent plumes is in its infancy, as the complex coupling of the multiple physical processes influencing plume evolution has proven enormously challenging to simulate. A few numerical studies of turbulent plumes using direct and large-eddy simulation, however, have appeared in the literature. Thus, Zhou *et al.* (2001) reported on a computational study of the near and far-field of a turbulent forced plume. Soteriou *et al.* (2002) studied the dynamics of pulsating instabilities in a planar plume using a high-resolution Lagrangian method. Chung & Devaud (2008) studied the near field of a helium plume with a modified k-epsilon Reynolds Averaged approach and with traditional eddy-viscosity LES methods. Pham *et al.* (2007) explored the relative performance of several variants of the dynamic Smagorinsky eddy-viscosity model in simulations of a turbulent plume, and concluded that no subgrid-scale (SGS) model was capable of capturing the inverse cascade of the Rayleigh-Taylor or Kelvin-Helmholtz instabilities that influence plume evolution.

Recently, DesJardin *et al.* (2004) explored the dynamics of buoyancy instability and vorticity in a large pool-fire configuration, and compared simulation results using existing

eddy-viscosity methods to the experimental study of O'Hern *et al.* (2005) of a 1-meter-diameter helium plume in the Sandia FLAME facility. The study focused on the adequacy of current eddy-viscosity subgrid models for simulating plume dynamics. The authors concluded that the principal source of error in the large-eddy simulations resulted from the failure of the traditional eddy-viscosity subgrid models to capture the inverse cascade of energy that gives rise to buoyancy-induced instabilities in the plume. Indeed, the authors specifically stated that

> *the net energy transfer in the near field is from small to large scales of turbulent motion, resulting in a net "upscale" transfer of turbulent energy. It is therefore unreasonable to expect that ... the existing SGS turbulence models that rely on a net downscale of energy transfer to perform well for this class of flows. To the contrary, the ideal SGS model for the near-field flow development would be to add energy ... to account for the effects of unresolved turbulence generation from baroclinic and gravitational torque* (DesJardin *et al.* 2004, at 1877).

The study closed by noting the pressing need for new subgrid models that incorporate buoyancy effects more directly, specifically the inverse cascade of energy that gives rise to buoyancy-induced instabilities near the plume base, and thus would more faithfully capture the complicated dynamics of the turbulent plume.

2. Numerical method

2.1. *The nLES method: multifractal modeling*

Given the limitations of current LES methods, the goal of the present work is to extend the recently developed Nonlinear LES (nLES) method (Burton 2008a,b; Burton & Dahm 2005a,b) to simulations of the turbulent plume. The nLES method represents a fundamental paradigm shift in turbulence modeling, away from eddy-viscosity subgrid methods that have directly hampered numerical study of turbulent plumes, as discussed above. Unlike eddy-viscosity LES approaches, the nLES method solves the original form of the filtered Navier-Stokes momentum equation, given by

$$\frac{\partial \overline{u}_i}{\partial t} + \frac{\partial}{\partial x_j}\,\overline{u_i\,u_j} \,+\, \frac{1}{\rho}\frac{\partial \overline{p}}{\partial x_i} \,-\nu\frac{\partial^2 \overline{u}_i}{\partial x_j^2} \,=0\,, \tag{2.1}$$

where the evolution of the resolved velocities $\overline{u}_i$, are dependent on the subgrid velocities u_i^{sgs} as

$$\overline{u_i\,u_j} \;\equiv\; \overline{\overline{u}_i\,\overline{u}_j} \,+\, \overline{\overline{u}_i\,u_j^{sgs}} \,+\, \overline{u_i^{sgs}\,\overline{u}_j} \,+\, \overline{u_i^{sgs}\,u_j^{sgs}}\,, \tag{2.2}$$

which are not directly known to the flow solver. By directly calculating the unclosed filtered nonlinear stresses, *e.g.* $\overline{u_i\,u_j}$, that appear in equation (2.1), the nLES method more directly incorporates the advective nonlinearities that drive actual hydrodynamic turbulence. No artificial viscosities or diffusivities of any kind are applied to the nLES system and no dealiasing is performed. Indeed, with this strategy, the nLES method stands as the only LES technique that can recover, with exceedingly high fidelity, the local instantaneous structure of *two-way* energy transfer – both forward transfer and backscatter – between the resolved and subgrid scales in an LES, with correlations exceeding $\rho \geq 0.99$ (Burton & Dahm 2005b). Thus, as inverse-energy transfer is essential

to the development of the turbulent plume, the nLES method holds the promise of substantially higher-fidelity numerical study of the plume and other buoyancy-driven flows.

The nLES method achieves this remarkable fidelity by drawing directly upon the significantly more complete understanding of turbulent flows that has developed in the half century since Smagorinsky (1963) introduced the eddy-viscosity approach that has come to dominate large-eddy simulation. In particular, the method makes use of multifractal scale-invariant structure of gradient-squared fields, such enstrophy $2\mathcal{Q} \equiv \omega \cdot \omega$ and scalar-energy dissipation $\chi \equiv D\nabla\phi \cdot \nabla\phi$, which exist at inertial range scales of turbulent flows (Sreenivasan 1991; Frederiksen *et al.* 1997; Burton & Dahm 2005a; Mullin & Dahm 2006). Using multifractal structure within the enstrophy field, an analytical model for the subgrid vorticity field $\omega^{sgs}(\mathbf{x}, t)$ can be developed. Then, using the Biot-Savart integral, the analytical model of the subgrid vorticity field can be inverted to recover an expression for the subgrid velocity field $u^{sgs}(\mathbf{x}, t)$ as

$$\mathbf{u}^{sgs}(\mathbf{x}) \;\equiv\; \frac{1}{4\pi} \int_{\mathbf{x}'} \omega^{sgs}(\mathbf{x}') \times \mathbf{K}(\,\mathbf{x},\, \mathbf{x}'\,)\;\, d^3\mathbf{x}', \tag{2.3}$$

where $\mathbf{K}(\,\mathbf{x},\, \mathbf{x}'\,) \equiv (\mathbf{x} - \mathbf{x}')/|\mathbf{x} - \mathbf{x}'|^3$ is the Biot-Savart kernel. The resulting expression for the subgrid velocities can be reduced through further analysis, to a form where the subgrid velocities $\mathbf{u}^{sgs}(\mathbf{x}, t)$ can be determined through a scaling transformation on the smallest resolved scale velocity component $\mathbf{u}^{\Delta}(\mathbf{x}, t)$, as

$$\mathbf{u}^{sgs}(\mathbf{x}, t) \approx \mathcal{B}\mathbf{u}^{\Delta}(\mathbf{x}, t)\,, \tag{2.4}$$

where, from the multifractal analysis, the scaling factor is given by

$$\mathcal{B} \sim 2^{-2\mathcal{N}/3} \left[\, 2^{4\mathcal{N}/3} - 1 \,\right]^{1/2}, \tag{2.5}$$

and where $\mathcal{N} \approx \log_2(\Delta/\lambda_\nu)$ is the number of cascade steps in the subgrid field of an individual LES grid-cell, estimated through the relation $\Delta/\lambda_\nu \sim Re_\Delta^{-3/4}$. The filtered inertial stress in the original filtered Navier-Stokes equation of (2.2) can then be approximated by

$$\overline{u_i\, u_j} \;\approx\; \overline{\overline{u}_i\, \overline{u}_j} + \mathcal{B}(\,\overline{\overline{u}_i\, u_j^{\Delta}} + \overline{u_i^{\Delta}\, \overline{u}_j}\,) + \mathcal{B}^2 \overline{u_i^{\Delta}\, u_j^{\Delta}}\,, \tag{2.6}$$

which is then used to update the velocity components in equation (2.1). For details of this derivation, see Burton & Dahm (2005a) .

An entirely analogous approach was used by Burton (2008a) to derive a model for the subgrid scalar concentrations $\phi^{sgs}(\mathbf{x}, t)$. In that study, the multifractal structure of the scalar dissipation field $\chi(\mathbf{x}, t) \;\equiv\; D\nabla\phi \cdot \nabla\phi(\mathbf{x}, t)$ was used to construct an analytical model of the subgrid scalar-gradient field $\nabla\phi^{sgs}(\mathbf{x}, t)$. Then, using a Green's function approach, this scalar-gradient field was inverted to recover an expression for the subgrid-scalar concentration field. In its final form, the model for $\phi^{sgs}(\mathbf{x}, t)$ involves a scaling transformation of the smallest-resolved scalar concentrations $\phi^{\Delta}(\mathbf{x}, t)$, as

$$\phi^{sgs}(\mathbf{x}, t) \;\approx\; \mathcal{D}\, \phi^{\Delta}(\mathbf{x}, t)\,, \tag{2.7}$$

where

$$\mathcal{D} \;\sim\; 2^{-\varphi\mathcal{N}/2} \left[\, 2^{\varphi\mathcal{N}} - 1 \,\right]^{1/2}, \tag{2.8}$$

and where $\varphi = 4/3$ at inertial-convective and $\varphi = 1$ at viscous-convective scales, respectively. Using these models, the evolution of the filtered scalar field thus involves solving

the original form of the filtered advection-diffusion equation, which is given by

$$\frac{\partial \overline{\phi}}{\partial t} + \frac{\partial}{\partial x_j}\overline{u_j\,\phi} - D\frac{\partial^2 \overline{\phi}}{\partial x_j \partial x_j} \;=\; 0\,, \tag{2.9}$$

by combining the multifractal models for the velocities (2.4) and scalars (2.7) as

$$\overline{u_j\,\phi} \;\equiv\; \overline{\overline{u}_j\,\overline{\phi}} + \mathcal{D}\,\overline{\overline{u}_j\,\phi^{\Delta}} + \mathcal{B}\,\overline{u_j^{\Delta}\,\overline{\phi}} + \mathcal{B}\,\mathcal{D}\,\overline{u_j^{\Delta}\,\phi^{\Delta}}\,. \tag{2.10}$$

By calculating the advective stresses in their original forms as filtered nonlinear products in equations (2.6) and (2.10), the nLES method more directly incorporates the advective nonlinearities that drive actual hydrodynamic turbulence. The nLES method thus better models the nonlinear mechanism responsible for most equilibrium-range transport of momentum, kinetic energy, scalar concentrations and scalar energy than traditional LES approaches that rely upon linear artificial viscous or diffusive closures.

2.2. *The nLES method: adaptive backscatter limiting*

In the nLES method, the physical models for the subgrid velocities and scalars, embodied in (2.4) and (2.7), are decoupled from the method used to control numerical errors during a simulation. Developed in Burton (2008a), adaptive backscatter limiting (ABL) controls resolved energy errors by reducing the magnitude of selected inertial stresses and scalar fluxes responsible for the backscatter of kinetic and scalar energies into the resolved field. For the momentum equation, ABL is implemented by scale separating the resolved strain-rate component field $\overline{S}_{(ij)}$ into two scale ranges, Δ and $\alpha\Delta$, where $\overline{S}_{(ij)} \equiv S^{\Delta}_{(ij)} + S^{\alpha\Delta}_{(ij)}$, and where generally $\alpha = 2$. Given that numerical errors in LES generally arise first at the smallest-resolved scales and propagate to the larger-resolved scales through nonlinear mode coupling, Burton (2008a) proposed that regions of erroneous kinetic energy transfer be identified where the ratio of strain-rate component magnitudes at the two scale ranges exceeds a certain threshold R_{th} as

$$R_{(ij)} \equiv \frac{|S^{\Delta}_{(ij)}|}{|S^{\alpha\Delta}_{(ij)}|} \;\geq\; R_{th}\,, \tag{2.11}$$

with R_{th} determined through a Kolmogorov analysis, and where the parentheses indicate that no summation is implied. When erroneously large Δ-scale gradients are detected at locations where kinetic energy is backscattering into the resolved scales, a local backscatter limiter $\mathcal{L}_{(ij)}$ can be defined as

$$\mathcal{L}_{(ij)} \;\equiv\; \frac{R_{th}}{R_{(ij)}}\,, \tag{2.12}$$

which then can be used to reduce the magnitude of the associated nonlinear inertial-stress component term, as

$$\widehat{\overline{u_{(i)}\,u_{(j)}}} \equiv \mathcal{L}_{(ij)}\,\overline{u_{(i)}\,u_{(j)}}\,. \tag{2.13}$$

It has been shown that applying these limited nonlinear stresses to update (2.1) cancels the erroneous backscatter detected with the metric of (2.11). An entirely analogous scalar-energy backscatter limiter is applied to control resolved errors in the scalar field that arise from calculation of equations (2.10) and (2.9). Using ABL, an nLES simulation manages resolved kinetic and scalar energy levels without the use of artificial-viscosities or -diffusivities that may unphysically distort the simulation, especially at the smallest-resolved scales that are most tightly coupled to the RT and KH instabilities that drive plume dynamics. A more detailed discussion of ABL can be found in Burton (2008a).

2.3. *Implementation in the NGA code*

For the present work, the nLES method has been implemented in the Center for Turbulent Research's NGA code. NGA is a three-dimensional structured finite-difference code that solves the low-Mach-number Navier Stokes equations using the fractional-step method of Kim & Moin (1985). The code employs high-accuracy variable-density energy-conserving finite-difference schemes of any order, which have been found suitable for the simulation of low-Mach-number turbulent flows as reported by Desjardins *et al.* (2008). For all present runs, second-order centered finite-difference operators for spatial derivatives and a third-order scheme for the time evolution were employed. The filtered density $\overline{\rho}$, viscosity $\overline{\mu}$ and kinematic diffusivity $\widetilde{D}$ were obtained through a mixing model, expressed as a function of a conserved mixture fraction which describes the gas mixture composition, and which is evolved through an advection-diffusion equation simultaneously with the velocity field. All species properties were then evaluated from a lookup table created with the FlameMaster code, as described by Blanquart *et al.* (2009).

2.4. *Simulation configuration*

The simulations have been configured to replicate the experimental helium-air plume study of O'Hern *et al.* (2005), and the computational study of the same configuration by DesJardin *et al.* (2004). In these studies, a one-meter diameter bulk inflow of helium was surrounded by an annular ring of width one-half meter, around which a small coflow of air was injected. Following the experimental setup, the simulation helium inlet velocity was set to $U_{inlet}^{He} \approx 0.325$m/sec, to which a zero-divergence fluctuation field of $\langle|0.003|\rangle$m/sec or 1% of the helium inflow velocity was added. The air coflow inlet was set to $U_{co}^{air} = 0.01$m/sec. The present simulations were run on a regular cylindrical grid (with no stretching factors) four meters in diameter and eight meters in the axial direction. Grid resolution was set at $N = 128 \times 64 \times 32$ with the axial velocity opposed to the gravity vector. The timestep was set to $\Delta t = 5 \times 10^{-4}$ giving a maximum CFL condition number near the outlet of the fully-developed plume as ≈ 0.45.

3. Results

The present report highlights only the initial evaluation of the nLES method in the helium-air plume configuration. The focus is here limited to the recovery of large-scale plume characteristics such as puffing rate and mean and fluctuating velocity and scalar distributions, using the current version of the nLES method. As discussed below in Section 4, it is anticipated that significant additional work will be undertaken in the future to extend the nLES method to higher-fidelity study of the turbulent plume.

Figure 1 illustrates a two-dimensional extract through the centerline of the density field from a single instant in an nLES simulation, showing the large-scale organization of the plume. Grayscale value black corresponds to pure helium, while white corresponds to pure ambient air. The figure shows Rayleigh-Taylor unstable bubbles rising from the plume base as heavier fluid is entrained toward the plume center. When this entrainment reaches a critical value, a burst of lighter fluid rises in the plume, propelled upward as a result of the buoyancy force arising from the density difference between the helium and air. The graphic illustrates the period near the beginning of such a puff cycle, immediately after an earlier concentration of helium has been released from the plume base and can be seen to be rising through the lower centerline of the plume.

The rate of puffing is a characteristic feature of most large-scale plumes, especially

FIGURE 1. Density field from helium plume simulation at $Re_D = 3000$ and $Ri = 76$ showing Rayleigh-Taylor unstable bubbles near plume base. The graphic shows the instant near the beginning of a puff cycle, with previous puff already rising from the plume base. Grayscale value black (white) is helium (air). Axial direction *(left to right)* is opposed to gravity vector.

those arising from the pool-fire configuration. The puffing cycle is tied to the rate at which the plume entrains ambient fluid from the surrounding environment and thus is principally responsible for feeding oxygen to such pool fires. As such, the puffing rate is critically important to determine the rate of fuel consumption in pool fires, and thus their duration and intensity. Furthermore, interruption of the puffing cycle may hold a key to controlling and ultimately extinguishing large scale pool fires (Tieszen 2001). Given this, it is critically important that the numerical method be able to recover the proper physics of the plume puffing cycle, including its frequency.

O'Hern (2005) reported a puffing frequency for the configuration of $f_p \approx 1.37\, sec^{-1}$, while Cetegen & Kasper (1996) found $f_p \approx 1.40\, sec^{-1}$ in a similar configuration. Finally, analytical work of Cetegen & Ahmed (1993) proposed that the puffing frequency of pool fires follows the relation $f_p = 1.5\sqrt{D_p}\, sec^{-1}$, where D_p is the plume inlet diameter. Using this metric in the present case, $f_p = 1.5\ sec^{-1}$. Figure 2 shows a typical trace of the axial velocity $\langle U \rangle$ timeseries signal on the centerline $x = 0.5m$ downstream of the plume inlet. The trace exhibits the periodic fluctuation of the mean axial velocity due to the puffing cycle described above. Power-series spectra from this timeseries shows a dominant mode of the puff at $f_p = 1.48\ sec^{-1}$, within 1% the analytical result of Cetegen & Ahmed (1993) and within 8% of the O'Hern results.

The distributions of mean velocities $\langle U_i \rangle$ and r.m.s. velocity fluctuations u_i' provide another means of assessing the accuracy of the nLES method. These distributions are examined as functions of the radial direction at 0.2, 0.4 and 0.6 meters downstream of the plume inlet, corresponding to those locations reported in the DesJardin (2004) study. In each graphic, the exact experimental value, originally from the O'Hern (2005) study, is given by the black dots $\cdots$; the experimental error bounds, as determined by the O'Hern study, are represented by the upper and lower dashed lines ---- ; and the nLES result is given by the solid black line —.

Figure 3 depicts *(left to right)* the radial distributions of the mean axial velocity $\langle U \rangle(r)$ at the three downstream locations. It is apparent that the nLES values fall within the

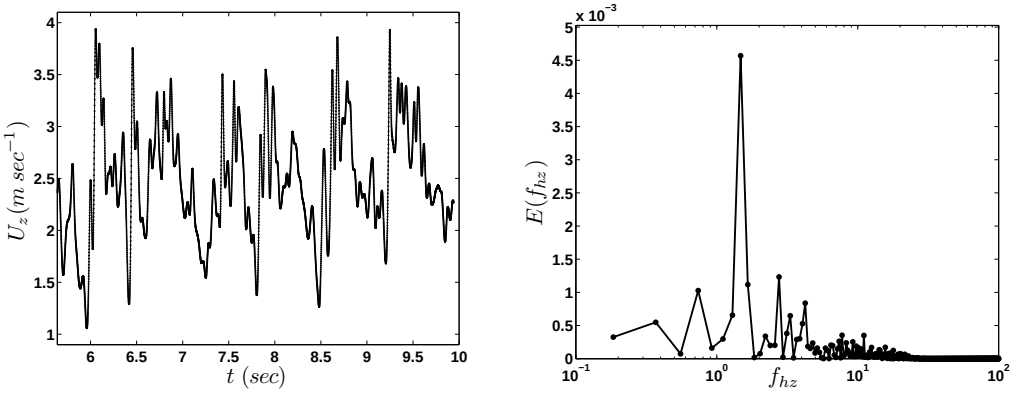

FIGURE 2. *(Left):* Timeseries signal of mean axial velocity $\langle U \rangle$ on centerline 0.5m downstream of plume inlet. *(Right):* Power spectrum of timeseries, showing dominant frequency of puff cycle as $f_p = 1.48\ sec^{-1}$.

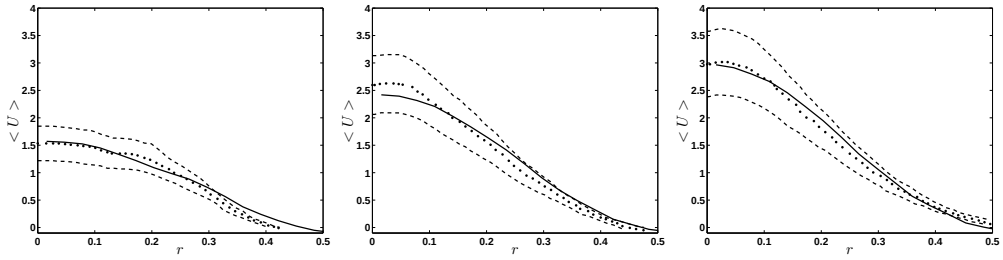

FIGURE 3. Mean streamwise velocity $\langle U \rangle$ as a function of radial distance r at *(left to right)*: 0.2m, 0.4m and 0.6m downstream of plume inlet. Experimental data (DesJardin *et al.* 2004): ····· ; experimental data uncertainty upper and lower bounds: – – – – ; nLES: ———

experimental error bounds at virtually all locations sampled and, in fact, nearly recover the exact experimental values at all three downstream locations. The mean radial velocity $\langle V \rangle(r)$ cross-stream distributions are depicted in figure 4. Near the centerline these distributions are captured with high accuracy. However, nLES values slightly exceed both experimental values and their error bounds at cross-stream locations $r > 0.25$m at all three downstream locations. The mean helium mass fraction $\langle Y^{He} \rangle(r)$ is depicted in figure 5. Here the distribution is slightly underpredicted near the centerline close to the plume base, but is within the experimental error bounds across the profiles at all three downstream locations. In addition, the mean value near the centerline is better predicted at each successive downstream location. However, the nLES profiles somewhat overpredict the exact experimental value at radial locations $r > 0.30$m.

Radial distributions of r.m.s. fluctuating quantities provide another means of assessing the accuracy of the nLES method. Figure 6 depicts radial distributions of u'_{rms} at the same three downstream locations. It is apparent that the nLES result underestimates the exact centerline rms values at all three locations, but falls within the experimental error bounds at most locations. In addition, the method somewhat overestimates values at radial distances $r \geq 0.3$ in the two nearest downstream locations. The method also captures some of the growth in the intensity of the fluctuations reported in the O'Hern (2005) study. The radial profiles of $v'_{rms}(r)$, the radial velocity fluctuation r.m.s., somewhat overpredict the experimentally reported values close to the centerline ($r \leq 0.2$) at

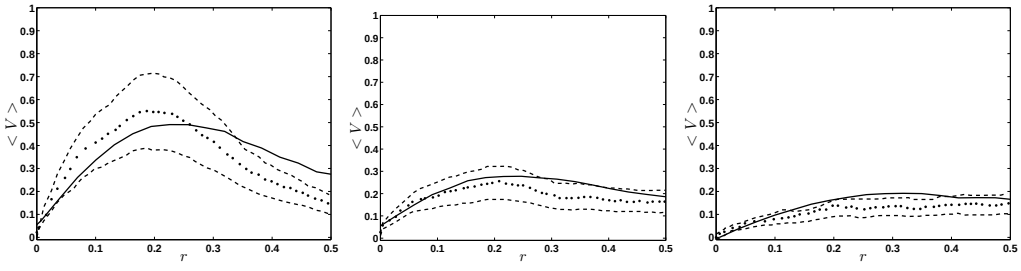

FIGURE 4. Same as Figure 3, but mean radial velocity $\langle V \rangle$.

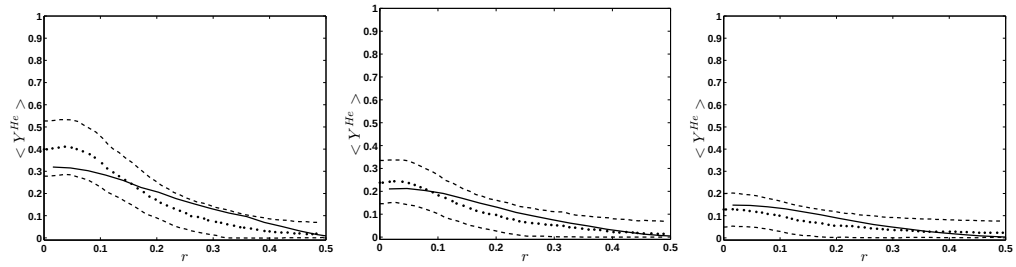

FIGURE 5. Same as Figure 3, but mean helium mass fraction $\langle Y^{He} \rangle$.

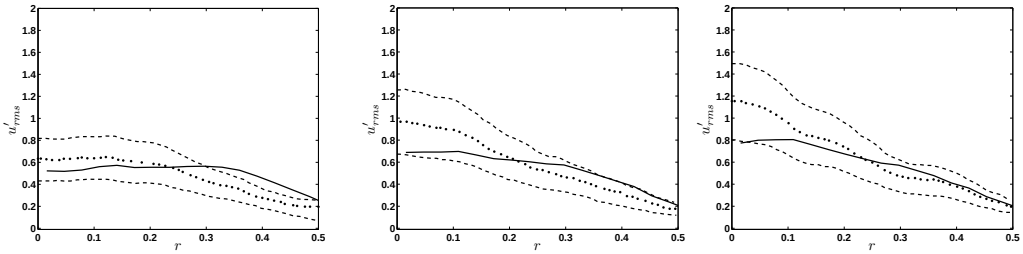

FIGURE 6. Same as Figure 3, but streamwise velocity r.m.s u'_{rms}.

the two nearest downstream locations, but fall within the experimental error bounds at the furthest downstream location sampled. However, for all three downstream locations the nLES method predicts the $v'_{rms}(r)$ distributions well at radial locations $r > 0.3m$.

The radial profiles of Y^{He}_{ms}, the helium mass-fraction fluctuation r.m.s., are shown in figure 7. At the nearest downstream location, the simulation slightly underpredicts the r.m.s fluctuations near the centerline for $r < 0.15$, while slightly overpredicting them at radial locations $r \geq 0.35$. At location $x = 0.4$m, the simulation also slightly underpredicts the r.m.s. values near the centerline, even though the results fall within the experimental error bounds at all $r \geq 0.15$. Finally, at $x = 0.6$m, the method better captures the fluctuations near the centerline $r \leq 0.18$m and near the simulation edges at $r \geq 0.4$m. In addition, the simulate captures decrease in r.m.s magnitude at successive downstream locations, even though these differences are not quite as pronounced as reported in the experimental data.

Figure 8 shows the centerline values of the mean axial velocity field $\langle U \rangle$ at five locations $x = 0.1,\ 0.2,\ 0.4,\ 0.5,\ 0.6$ m in the plume far field. Exact experimental values from O'Hern (2005) are indicated by the black circles, experimental error bars are indicated by the black lines, and the nLES results are indicated by the black diamonds. At all

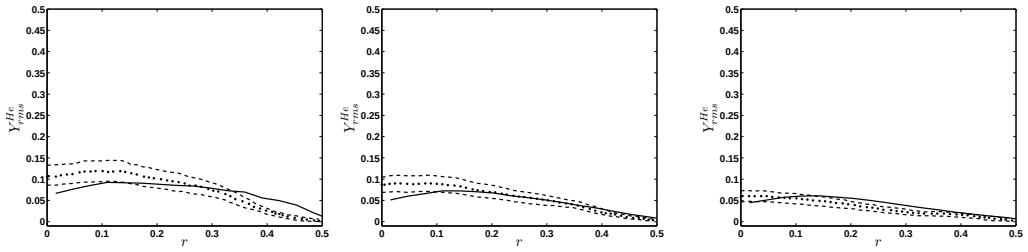

FIGURE 7. Same as Figure 3, but helium mass fraction r.m.s. Y^{He}_{rms}.

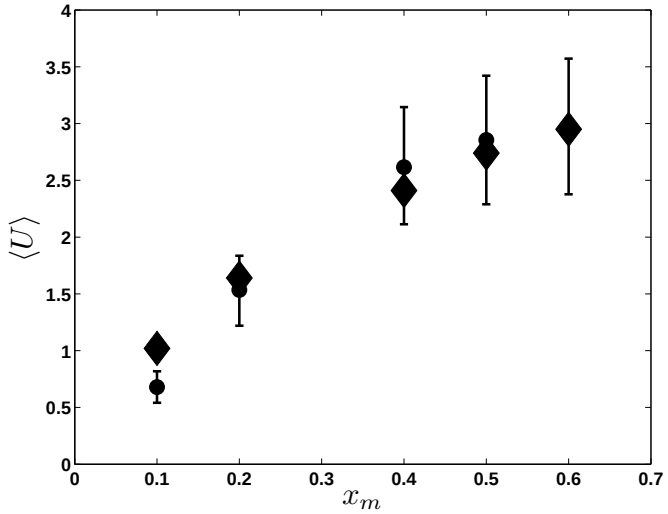

FIGURE 8. Mean axial velocity $\langle U \rangle$ values at five centerline locations in the plume, $x = 0.1,\ 0.2,\ 0.4,\ 0.5,\ 0.6$ m. Experimental values: *black circles*; Experimental error bars: *black lines*; nLES results: *black diamonds*. The nLES method well captures the increase in mean axial velocity with downstream distance due to buoyancy forces in the plume as reported in O'Hern (2005).

downstream locations except the first at $x = 0.1$m, the nLES method closely recovers the exact experimental values reported by O'Hern, indicating that the acceleration of the helium-air mixture by the buoyancy forces is well captured by the nLES method.

4. Future work

The foregoing reports only the results of the initial validation of the implementation of the nLES method into the CTR's low-Mach number variable-density code, NGA. Significant additional work is currently in progress to more fully assess the accuracy of the nLES method in its present form and to better adapt it to buoyancy-driven turbulent flows like the plume. Validation of these improvements will focus on better estimation of the field distributions discussed in the present report. Direct comparisons will be made with simulations run with NGA, but using the dynamic Smagorinsky model (Germano *et al.* 1991). In addition, given the nLES method's unique ability to recover the subgrid energy production field, the work will investigate the physical mechanism for reverse

energy transfer due to Rayleigh-Taylor and Kelvin-Helmholtz instabilities and their interaction with vorticity production and transport in the plume. A clearer understanding of these processes has been recognized as essential to better understanding the dynamics of plume evolution. It is hoped that the new physical understanding gained will motivate new strategies to control large-scale industrial pool fires, which are estimated to cause billions of dollars of damage each year in the United States alone (Tieszen 2001).

Acknowledgments

The author is grateful for a number of discussions with Professors P. Moin and G. Iaccarino on this project, as well as to G. Blanquart, E. Knudsen, M. Shashank, R. Mittal and C. Schmidt for their help answering a variety of questions during the implementation of the nLES method in the NGA code.

REFERENCES

Blanquart, G., Pepiot-Desjardins, P. & Pitsch, H. 2009 Assessing uncertainties in numerical simulations of simple reacting flows using the FlameMaster code. *Comb. Theory Model.*, in preparation.

Burton, G. C. 2008 The nonlinear large-eddy simulation method (nLES) applied to $Sc \approx 1$ and $Sc \gg 1$ passive-scalar mixing. *Phys. Fluids* **20**, 035103.

Burton, G. C. 2008 Scalar-energy spectra in simulations of $Sc \gg 1$ mixing by turbulent jets using the nonlinear large-eddy simulation method. *Phys. Fluids* **20**, 071701.

Burton, G. C. & Dahm, W. J. A. 2005 Multifractal subgrid-scale modeling for large eddy simulation. Part I: Model development and *a priori* testing. *Phys. Fluids* **17**, 075111.

Burton, G. C. & Dahm, W. J. A. 2005 Multifractal subgrid-scale modeling for large eddy simulation. Part II: Backscatter limiting and *a posteriori* evaluation. *Phys. Fluids* **17**, 075112.

Cetegen, B. M. & Ahmed, T. A. 1993 Experiments on the periodic instability of buoyant plumes and pool fires. *Combust. Flame* **93**, 157.

Cetegen, B. M. & Kasper, K. D. 1996 Experiments on the oscillatory behavior of buoyant plumes of helium and helium-air mixtures. *Phys. Fluids* **8**, 2974-2984.

Chung, W. & Devaud, C. B. 2008 Buoyancy-corrected κ-ε models and large-eddy simulation applied to a large axisymmetric helium plume. *Intl. J. Num. Meth. Fluids* 10.0012/fld.1720.

DesJardin, P. E., O'Hern, T. J. & Tieszen, S. R. 2004 Large eddy simulation and experimental measurements of the near-field of a large turbulent helium plume. *Phys. Fluids* **16**, 1866-1883.

Desjardins, O., Blanquart, G., Balarac, G. & Pitsch, H. 2008 High order conservative finite difference scheme for variable density low Mach number turbulent flows. *J. Comp. Phys.* **227**, 71257159.

Frederiksen, R. D., Dahm, W. J. A. & Dowling, D. R. 1997 Experimental assessment of fractal scale similarity in turbulent flows. Part 3. Multifractal scaling. *J. Fluid Mech.* **338**, 127-155.

Germano, M., Piomelli, U., Moin, P. & Cabot, W. H. 1991 A dynamic subgrid-scale eddy viscosity model. *Phys. Fluids* **A 3**, 1760-1765.

Kim, J. & Moin, P. 1985 Application of a fractional step method to the incompressible Navier-Stokes equations. *J. Comp. Phys.* **59**, 308-323.

Mullin, J. A. & Dahm, W. J. A. 2006 Dual-plane stereo particle image velocimetry measurements of velocity gradient fields in turbulent shear flow. II. Experimental results. *Phys. Fluids* **18**, 035102.

O'Hern, T. J., Weckman, E. J., Gerhart, A. L., Tieszen, S. R. & Schefer, R. W. 2005 Experimental study of a turbulent buoyant helium plume. *J. Fluid Mech.* **544**, 143-171.

Pham, M. V., Plourde, F. & Doan, K. S. 2007 Direct and large-eddy simulations of a pure thermal plume. *Phys. Fluids* **19**, 025103.

Smagorinsky, J. 1963 General circulation experiments with the primitive equations: I. The basic equations. *Mon. Weather Rev.* **91**, 99-164.

Soteriou, M.C., Dong, Y. & Cetegen, B. M. 2002 Lagrangian simulation of unsteady near-field dynamics of planar buoyant plumes. *Phys. Fluids* **14**, 3118-3133.

Sreenivasan, K. R. 1991 Fractals and multifractals in fluid turbulence. *Annu. Rev. Fluid. Mech.* **23**, 539-600.

Tieszen, S. R. 2001 On the fluid mechanics of fires. *Annu. Rev. Fluid. Mech.* **33**, 67-92.

Zhou, X., Luo, K. H. & Williams, J. J. R. 2001 Large eddy simulation of a turbulent forced plume. *Eur J. Mech. B/Fluids.* **20**, 233-250.